
**ASTRONOMY, ASTROPHYSICS,
AND COSMOLOGY**

Theoretical Reconstruction of the Parameters of Gas Emitting in the Spectral Lines of the Optical Range of Hydrogen, Helium, and Calcium during the SOL2015-10-01 Flare

V. A. Maliutin^{1*}, Yu. A. Kupryakov^{2,3**}, K. V. Bychkov², A. B. Gorshkov², and O. M. Belova⁴

¹*Department of Astrophysics and Stellar Astronomy, Faculty of Physics, Lomonosov Moscow State University,
Moscow, 119991 Russia*

²*Sternberg Astronomical Institute, Lomonosov Moscow State University, Moscow, 119234 Russia*

³*Astronomical Institute of the Czech Academy of Sciences, Ondřejov, 251 65 The Czech Republic*

⁴*Department of Experimental Astronomy, Faculty of Physics, Lomonosov Moscow State University,
Moscow, 119991 Russia*

Received September 26, 2024; revised October 15, 2024; accepted October 25, 2024

Abstract—The solar flare SOL2015-10-01 was observed at the Astronomical Institute of the Czech Academy of Sciences using the HSFA-2 horizontal solar research setup. After processing the spectra, the integral radiation fluxes were determined for the H α , H β , and H ϵ lines of hydrogen, the D3 line of helium, as well as the resonance $\lambda = 3968 \text{ \AA}$ and infrared $\lambda = 8542 \text{ \AA}$ lines of the CaII ion. The analyzed flare exhibited two characteristic cores, and during processing, the fluxes from each core were determined. Within the framework of the heated gas model, theoretical calculations of plasma parameters were performed, taking into account the physical conditions in the chromosphere, including self-absorption in the spectral lines. The simultaneous analysis of six lines from three atomic systems made it possible to reconstruct the temperature, density, and spatial structure of the emitting gas with high confidence. A strong temperature inhomogeneity in the emitting gas was revealed. The reconstructed theoretical gas concentration values exceed those for prominences by at least an order of magnitude, suggesting the chromospheric nature of the emitting gas.

Keywords: chromosphere, spectral lines, radiation flux, heated gas model

DOI: 10.3103/S0027134925700110

INTRODUCTION

The radiation of solar flares in the spectral lines of the optical range of atoms and first ions of chemical elements makes it possible to determine the parameters of the emitting gas under conditions close to those of the chromosphere. The populations of discrete energy levels and the ionization state of the gas in these conditions can significantly differ from their equilibrium values. The most significant contribution to the ionization rate of chromospheric gas can come from sufficiently excited levels within the principal quantum number range $8 < N < 16$. Therefore, a sufficiently comprehensive set of atomic data and the ability to account for discrete states with large N values are necessary. Both of these requirements were considered in our calculations, distinguishing them

from codes such as RADYN [1–4], where levels with $N < 6$ (for hydrogen) and $N < 5$ (for helium atoms and CaII ions) are considered.

Flare processes in the chromosphere are highly diverse. In RADYN [3], a beam of nonthermal electrons with a power-law energy spectrum is considered as the energy source of the flare. Within the described approximations, researchers use the RADYN package to interpret observed lines, such as H α and neutral iron lines [5], as well as H α and the Ca IR line ($\lambda = 8542 \text{ \AA}$) [6, 7].

The work [8] investigates the influence of the hydrogen resonance series on the photoionization of CaII levels. Calculations are performed in two modes: with and without the consideration of Lyman quanta. The RADYN code and the modular software package LightWeaver were applied. Accounting for photoionization by Lyman quanta alters both the formation

*E-mail: malyutin@list.ru

**E-mail: jurij.kupriakov@asu.cas.cz

Table 1. Observed fluxes from core A (erg/s/cm²). Time moments are given in UT

UT	13 : 09 : 59	13 : 10 : 38	13 : 11 : 06	13 : 12 : 31	13 : 14 : 23	13 : 15 : 44
H α	2.82×10^7	3.47×10^7	5.09×10^7	3.54×10^7	1.15×10^7	6.69×10^6
H β	2.50×10^7	3.47×10^7	4.99×10^7	4.12×10^7	9.22×10^6	4.40×10^6
H ϵ	1.47×10^7	2.17×10^7	2.55×10^7	2.01×10^7	1.30×10^7	9.29×10^6
H CaII	1.61×10^7	2.30×10^7	2.61×10^7	2.46×10^7	1.64×10^7	1.49×10^7
IR CaII	5.40×10^6	7.57×10^6	1.14×10^7	1.09×10^7	3.54×10^6	2.46×10^6
D3	1.51×10^6	2.38×10^6	4.41×10^6	3.03×10^6	3.27×10^5	–

Table 2. Same as Table 1, but for core B

UT	13 : 09 : 59	13 : 10 : 38	13 : 11 : 06	13 : 12 : 31	13 : 14 : 23	13 : 15 : 44
H α	4.18×10^7	4.16×10^7	4.48×10^7	3.79×10^7	1.77×10^7	1.76×10^7
H β	3.19×10^7	4.16×10^7	4.64×10^7	3.41×10^7	1.21×10^7	8.38×10^6
H ϵ	1.48×10^7	2.28×10^7	2.64×10^7	1.52×10^7	1.17×10^7	7.09×10^6
H CaII	1.67×10^7	2.39×10^7	2.64×10^7	2.16×10^7	1.58×10^7	1.37×10^7
IR CaII	1.04×10^7	1.01×10^7	1.18×10^7	1.32×10^7	7.10×10^6	6.78×10^6
D3	3.38×10^6	3.69×10^6	4.41×10^6	2.06×10^6	8.58×10^5	–

region and the profile of the CaII IR line ($\lambda = 8542 \text{ \AA}$). The calculations showed that the effect of Lyman quanta on the CaII H line is much weaker.

This work is a continuation of the study described in the paper “Observation of the Solar Flare SOL2015-10-01 and Calculation of Its Emission Using the Heated Layer Superposition Model” [9], where we investigated the optical lines of hydrogen, helium, and the CaII ion.

1. OBSERVATIONS

The SOL2015-10-01 flare in active region NOAA 12422 with coordinates S18 W66 (M4.5 flare class) was observed using the HSFA-2 spectrograph (Ondřejov Observatory). This spectrograph allows for simultaneous observations in the CaII H, H ϵ , H β , D3, H α , and Ca IR 8542 \AA lines. The flare was observed in all these lines. Unlike in our previous work, we were able to isolate the flux of the H ϵ line. As an example, Fig. 1 shows an image of the chromosphere and the spectrum in the H α line at 13 : 10 : 38 UT. The dark horizontal lines, corresponding to a separation of 53 800 km on the Sun, are used to align the obtained spectra with the slit-jaw image. The flare exhibited two cores, marked in the image as A and B. Photometry was performed in the regions marked with white rectangles.

After considering flat-field and dark-field frames, line profiles were constructed taking into account the chromospheric background emission (see an example in Fig. 2), and the radiation fluxes were determined (Fig. 3, Tables 1 and 2). At 13 : 15 : 44 UT, the helium line was observed in absorption; therefore, fluxes for this moment are not presented. It should be noted that in [9], we previously presented data for 13 : 10 : 38 UT; it can be seen that the integral fluxes from the two cores in Table 1 of the previous work are comparable to and even smaller (for H β and H α) than the fluxes from a single core (Tables 1 and 2 of the current work). These differences are due to refined observation reductions.

2. CALCULATION TECHNIQUE

In this work, we focused on the consideration of gas layers with specific values of thickness L , concentration N , temperature T , and turbulent velocity v . The layers are arranged perpendicular to the line of sight, with the farthest layer from the observer considered as the first. The parameters and number of layers were selected to minimize the difference between theoretical and observed fluxes in the spectral lines. The calculations accounted for all major processes of level population and depopulation in the plasma, which, generally speaking, is not transparent at the frequencies of spectral lines. Photospheric

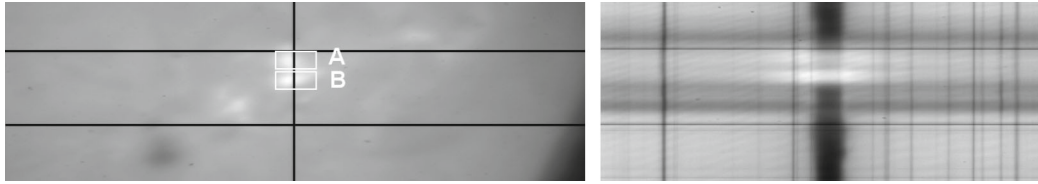


Fig. 1. Left: Active region NOAA 12422 with cores A and B (marked with white rectangles); Right: spectrum in the H α line (wavelengths increase to the right).

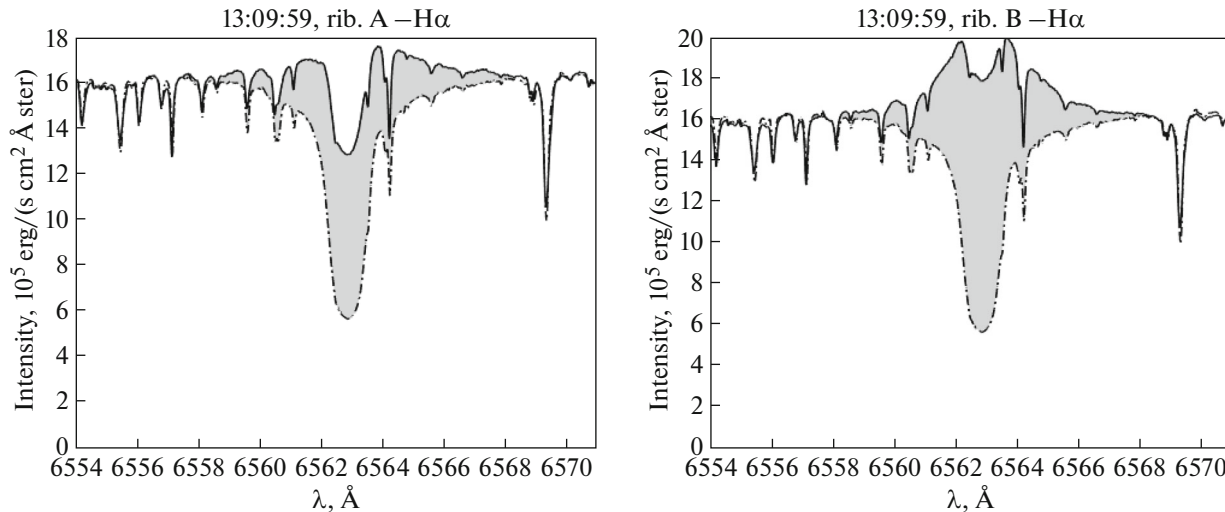


Fig. 2. Profiles of the H α line: Left—core A, right—core B at 13 : 09 : 59 UT. The shaded area of the profile corresponds to the integral flux.

radiation was modeled as blackbody radiation with a temperature of 5400–5500 K, corresponding to the temperature of the penumbra of a sunspot [9]. In addition to photospheric radiation, chromospheric emission lines of the hydrogen resonance series above Ly β contribute to the photoionization of CaII [8]. The effect of Lyman lines on the photoionization of CaII was also modeled within the blackbody radiation approximation with a corresponding temperature T_{Ly} . Line transfer was taken into account within the escape probability approximation [10–12]. The profiles of helium atom and calcium ion lines were considered as Voigt profiles, while hydrogen line profiles were treated as convolutions of Doppler and Holtsmark profiles. A detailed description of the calculation method is provided in [13]. The atomic data used in the calculations are thoroughly described in [14]. For the hydrogen atom, 18 discrete levels are considered; for helium, 29 levels (up to the principal quantum number $N = 5$); and for CaII in the current work, 22 discrete levels (up to the principal quantum number $N = 10$) are included.

3. CALCULATION RESULTS

Tables 3 and 4 present two to four gas parameters for each time moment, with indices corresponding

to the number of the emitting layer. Tables 5 and 6 provide the corresponding theoretical fluxes. By comparing Table 1 and Table 5, which describe core A, and Table 2 and Table 6, which describe core B, we can see that in most cases, a set of theoretical fluxes in the spectral lines close to the observed values was achieved. The simultaneous presence of six lines with different excitation energies in the spectra indicates a significant inhomogeneity of the emitting gas along the line of sight.

3.1. Helium Emission

The emission in the helium line forms in the hottest layer and is highly sensitive to both the temperature and concentration of this layer. A deviation of these values from the optimal ones by 1% can result in a 10% increase or decrease in the helium line flux. In this sense, helium emission serves as a good marker of the hottest layer. The moment 13 : 14 : 23(A) is the only case where a significant portion of the flux in the D3 line originates directly from the third and fourth layers (with temperatures of $T = 15\,000$ and $18\,000$ K; see Table 3).

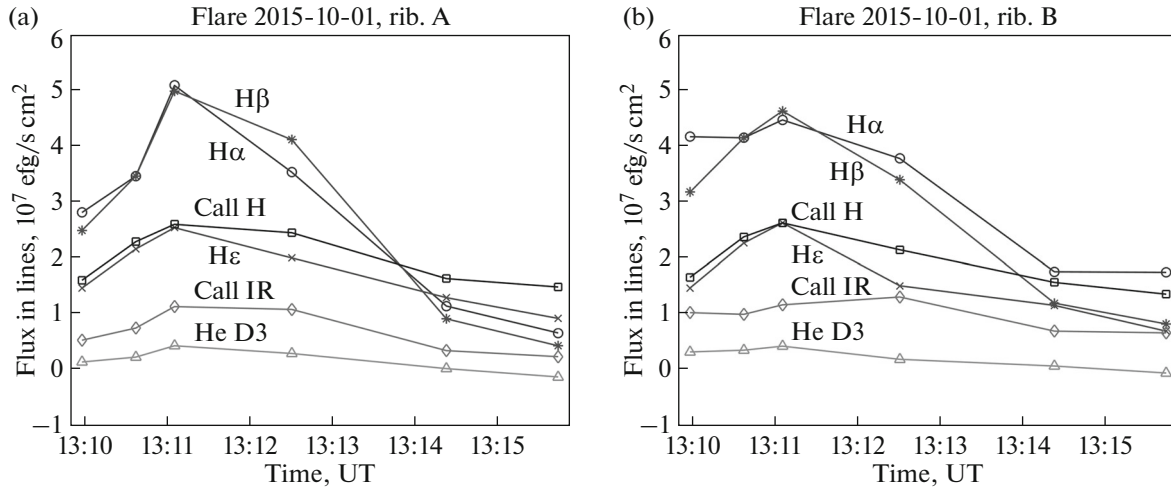


Fig. 3. Temporal variation of fluxes (in erg/s cm^2) in the six registered lines: (a) fluxes from core A; (b) fluxes from core B.

Table 3. Parameters of the emitting layers of core A in the active region. The lowest parameter index corresponds to the farthest layer, while the highest index corresponds to the layer closest to the observer. Time moments are given in UT. Gas concentration N is in cm^{-3} , layer thickness L in 10^3 km, gas temperature T and T_{Ly} in K, and turbulent velocity v in km/s

UT	13 : 09 : 59	13 : 10 : 38	13 : 11 : 06	13 : 12 : 31	13 : 14 : 23	13 : 15 : 44
N_1, cm^{-3}	7.25×10^{11}	1.12×10^{12}	1.18×10^{12}	1.03×10^{12}	7.60×10^{11}	2.40×10^{12}
N_2	5.00×10^{11}	1.10×10^{11}	1.10×10^{11}	3.00×10^{11}	9.00×10^{11}	1.50×10^{12}
N_3		1.12×10^{12}	8.50×10^{12}	1.40×10^{12}	4.00×10^{10}	3.00×10^{11}
N_4					5.20×10^{10}	1.00×10^{11}
$L_1, 10^3$ km	15	10	10	10	20	25
L_2	5	6	6	5	25	25
L_3		1.2	1	1	2.6	15
L_4					5	4
T_1, K	12 320	12 520	12 900	12 750	8800	7000
T_2	4800	6500	6000	6000	6500	11 300
T_3		4500	6100	6000	15 000	9000
T_4					18 000	5500
$v_1, \text{km/s}$	150	180	240	224	175	150
v_2	132	135	240	185	70	85
v_3		165	245	145	120	40
v_4					70	38
T_{Ly}, K	7280	7290	7160	6870	7900	9230

3.2. Hydrogen Emission

Let us analyze the emission in the Balmer lines. At the moment 13 : 09 : 59(A), a shallow decrement is observed ($F(\text{H}\alpha)/F(\text{H}\beta) = 1.12$, $F(\text{H}\epsilon)/F(\text{H}\beta) =$

0.59) with moderate absolute fluxes ($F(\text{H}\alpha)$, $F(\text{H}\beta) < 3 \times 10^7 \text{ erg/s cm}^2$). To explain these data, it was sufficient to consider two layers. The $\text{H}\beta$ line is at the transparency threshold, while the $\text{H}\alpha$ line is

Table 4. Same as Table 3, but for core B

UT	13 : 09 : 59	13 : 10 : 38	13 : 11 : 06	13 : 12 : 31	13 : 14 : 23	13 : 15 : 44
N_1, cm^{-3}	4.00×10^{12}	1.12×10^{12}	1.21×10^{12}	8.85×10^{11}	1.10×10^{12}	4.10×10^{11}
N_2	4.00×10^{11}	1.10×10^{11}	4.50×10^{11}	3.00×10^{11}	1.00×10^{11}	5.00×10^{11}
N_3	6.40×10^{11}	4.20×10^{12}	4.40×10^{12}	2.00×10^{12}		8.50×10^{10}
N_4	8.00×10^{11}					2.20×10^{12}
$L_1, 10^3 \text{ km}$	25	10	10	10	9.8	15
L_2	10	6	5	5	2.8	15
L_3	10	1.5	1	1		3
L_4	10					1
T_1, K	4000	12 800	12 860	12 640	11 950	9900
T_2	14 000	6500	6000	6200	6500	8600
T_3	10 000	6100	5900	6400		19 200
T_4	6500					4000
$v_1, \text{km/s}$	120	215	240	190	65	230
v_2	180	200	200	190	155	72
v_3	205	208	220	190		32
v_4	260					165
T_{Ly}, K	7850	7340	7050	6570	7360	7050

Table 5. Theoretical fluxes of core A (erg/s cm^2). Time moments are given in UT

UT	13 : 09 : 59	13 : 10 : 38	13 : 11 : 06	13 : 12 : 31	13 : 14 : 23	13 : 15 : 44
H α	2.74×10^7	3.43×10^7	5.05×10^7	3.67×10^7	1.21×10^7	6.69×10^6
H β	2.38×10^7	3.44×10^7	4.90×10^7	4.19×10^7	9.29×10^6	4.39×10^6
H ϵ	1.39×10^7	2.20×10^7	2.57×10^7	2.05×10^7	1.14×10^7	9.30×10^6
H CaII	1.69×10^7	2.37×10^7	2.51×10^7	2.38×10^7	7.93×10^6	1.13×10^7
IR CaII	5.35×10^6	7.47×10^6	1.12×10^7	1.05×10^7	3.56×10^6	2.48×10^6
D3	1.49×10^6	2.39×10^6	4.47×10^6	3.03×10^6	3.20×10^5	–

opaque. In the first layer, strong emission with a steep decrement forms, while the second layer significantly attenuates the flux in the H α line, only slightly altering the H β line and having no effect on the H ϵ line. At the moment 13 : 09 : 59(B), the decrement is relatively shallow $F(\text{H}\alpha)/F(\text{H}\beta) = 1.31$, and the H ϵ line is relatively bright: $F(\text{H}\epsilon)/F(\text{H}\beta) = 0.49$. The main emission forms in the second and third layers, while the fourth layer blocks excess flux in H α .

The six observations from 13 : 10 : 38 to 13 : 12 : 31(A, B) are very similar in terms of Balmer line formation. In the first layer (dense and hottest), strong

emission forms in the H α and H β lines, along with the required flux in the H ϵ line. The second and third layers contribute little to the H ϵ line but attenuate the flux in the H α and H β lines from the first layer while contributing their own flux to these lines, leveling the fluxes: $F(\text{H}\alpha) \approx F(\text{H}\beta)$.

The time moments 13 : 14 : 23(A)–13 : 15 : 44(A) are characterized by significantly lower absolute fluxes: $F(\text{H}\epsilon) > F(\text{H}\alpha) > F(\text{H}\beta)$. The H ϵ line is at the transparency threshold, while the H β and H α lines are opaque. Despite only five measured lines being present at 13 : 15 : 44, explaining such

Table 6. Same as Table 5, but for core B

UT	13 : 09 : 59	13 : 10 : 38	13 : 11 : 06	13 : 12 : 31	13 : 14 : 23	13 : 15 : 44
H α	4.09×10^7	4.24×10^7	4.49×10^7	3.79×10^7	1.87×10^7	1.96×10^7
H β	3.13×10^7	4.17×10^7	4.68×10^7	3.42×10^7	1.30×10^7	8.37×10^6
H ϵ	1.52×10^7	2.29×10^7	2.66×10^7	1.55×10^7	1.23×10^7	7.43×10^6
H CaII	1.61×10^7	2.35×10^7	2.61×10^7	2.12×10^7	1.48×10^7	1.28×10^7
IR CaII	1.06×10^7	9.96×10^6	1.17×10^7	1.31×10^7	7.11×10^6	7.38×10^6
D3	3.36×10^6	3.61×10^6	4.39×10^6	2.08×10^6	8.47×10^5	—

Table 7. Comparison of optical and X-ray fluxes and radiation powers. F(X), F(A), F(B) represent the X-ray flux in the 1–8 Å band from GOES data, adjusted to near-Earth space; the total flux from core A and the total flux from core B in the six studied lines, adjusted to the chromosphere (erg/s cm²). L(X), L(A), L(B) represent the corresponding powers (erg/s)

UT	13 : 09 : 59	13 : 10 : 38	13 : 11 : 06	13 : 12 : 31	13 : 14 : 23	13 : 15 : 44
F(X)	4.5×10^{-2}	5.0×10^{-2}	4.9×10^{-2}	3.4×10^{-2}	2.2×10^{-2}	1.6×10^{-2}
F(A)	9.1×10^7	1.2×10^8	1.7×10^8	1.4×10^8	5.4×10^7	3.9×10^7
F(B)	1.2×10^8	1.4×10^8	1.6×10^8	1.2×10^8	6.5×10^7	5.4×10^7
L(X)	1.3×10^{26}	1.4×10^{26}	1.4×10^{26}	9.6×10^{25}	6.2×10^{25}	4.5×10^{25}
L(A)	3.3×10^{26}	4.3×10^{26}	6.1×10^{26}	5.0×10^{26}	1.9×10^{26}	1.4×10^{26}
L(B)	4.3×10^{26}	5.0×10^{26}	5.8×10^{26}	4.3×10^{26}	2.3×10^{26}	1.9×10^{26}

a decrement required four gas layers. The farthest layer is now cold, while the hotter ones lie closer to the observer. More than one layer contributes significantly to the H ϵ flux. The turbulent velocity in the upper layers (second, third, and fourth) is $v \leq 120$ km/s, lower than in previous cases, resulting in significant absorption in the H α and H β lines, a steep decrement $F(\text{H}\alpha) > F(\text{H}\beta)$, and some attenuation of H ϵ . As a result of this attenuation, at the moment 13 : 14 : 23(A), the theoretical H ϵ flux turned out to be slightly lower than the H α flux. The moments 13 : 14 : 23(B)–13 : 15 : 44(B) are similarly characterized by lower absolute fluxes and a steep decrement $F(\text{H}\alpha) > F(\text{H}\beta) \sim F(\text{H}\epsilon)$. At the moment 13 : 14 : 23(B), the emission can be explained by a combination of two layers, with the farthest layer providing the H ϵ flux, while the upper layer absorbs the H α line and ensures the required ratio of all three fluxes. At the moment 13 : 15 :

44(B), the third layer is the hottest of the four layers, but it contributes less to the H ϵ flux compared to the first and second layers.

3.3. Emission of the Calcium Ion

The fluxes in the two calcium ion lines significantly contribute to refining the stratification of gas layers. The infrared line remains optically thin and is highly sensitive to changes in the gas layer temperature, T_{Ly} , and the layer concentration. The resonance line, being optically thick, is primarily sensitive only to variations in T_{Ly} . In both cores, a large portion of calcium emission originates in the hot layers, while in the upper layers, the flux in the resonance line is substantially blocked, and the emission in the infrared line either slightly increases or remains unchanged.

Cool outer layers with temperatures $T \leq 6500$ K helped enhance the transparency of the CaII H line

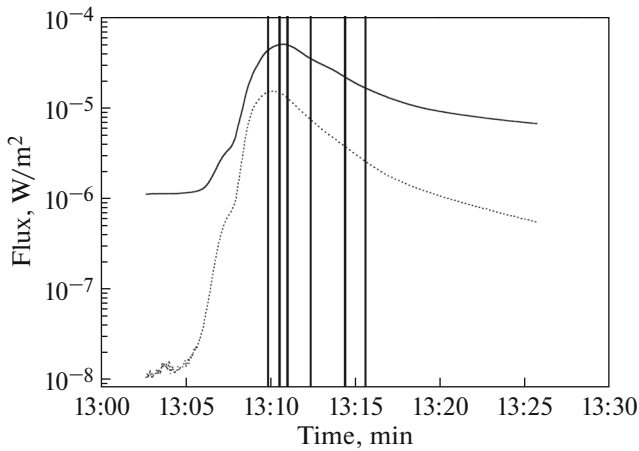


Fig. 4. X-ray flux curves from GOES data (W/m^2) as a function of time. The upper solid curve corresponds to the 1–8 Å range, and the lower dotted curve corresponds to the 0.5–4 Å range. Vertical lines mark the moments of optical flux measurements from Tables 1, 2.

and increased the theoretical flux to values comparable to those observed. An exception is the moment 13 : 14 : 23(A), where the resonance line in the calculations is suppressed by a factor of two compared to the observed flux, and the moment 13 : 15 : 48(A), where it is suppressed by one-quarter. Attempts to increase the theoretical flux in the CaII H line by varying the parameters of the existing layers result in a disruption of the Balmer decrement, while adding new layers only leads to further suppression of this line.

3.4. Comparison with X-ray Flux

Table 7 presents a comparison of fluxes and powers in the optical lines and the GOES X-ray band (1–8 Å). Figure 4 shows a graph of the solar X-ray flux over time with six highlighted moments corresponding to our optical observations.

The X-ray radiation power was calculated from the flux at the Earth's surface ($F(X)$ in Table 7) by multiplying it by the surface area of a sphere with a radius equal to the Earth's orbital semimajor axis ($a_{\oplus} = 1.5 \times 10^8$ km). The optical radiation power was calculated by multiplying the fluxes ($F(A)$, $F(B)$ in Table 7) by the areas of the rectangles surrounding the luminous cores shown in Fig. 1 (left). The dimensions of these rectangles are $12\,000 \times 30\,000$ km. The X-ray radiation power ($L(X)$ in Table 7) was found to be several times weaker than the optical radiation power ($L(A)$, $L(B)$ in Table 7), indicating that X-ray radiation cannot serve as the primary energy source for emission in the optical lines.

CONCLUSIONS

The main conclusions of this work are as follows:

1. Within the applied method, it was possible in most cases to obtain a set of theoretical fluxes in the spectral lines that closely matched the observed values.
2. The simultaneous presence in the flare core spectra of the D3 helium line (high excitation), the 3968 Å resonance line of the calcium ion, and its 8542 Å infrared line (low excitation), combined with the unique flux ratios in the Balmer series lines, indicates significant inhomogeneity in the emitting gas. The reconstructed parameters showed that each episode contains layers with temperatures ranging from high (12 000 K–18 000 K) to low (4500 K–5500 K) and concentrations ranging from 10^{11} to 10^{12} cm^{-3} .
3. The reconstructed theoretical density values exceed the gas density in prominences by at least an order of magnitude, supporting the hypothesis of the chromospheric nature of the cores.

ACKNOWLEDGMENTS

The authors express their gratitude to the GOES and Ondřejov Observatory teams for providing the opportunity to conduct observations and use their data.

FUNDING

This work was supported by ongoing institutional funding. No additional grants to carry out or direct this particular research were obtained.

CONFLICT OF INTEREST

The authors of this work declare that they have no conflicts of interest.

REFERENCES

1. M. Carlsson and R. F. Stein, in *Proceedings of a Mini-Workshop on Chromospheric Dynamics*, Ed. by M. Carlsson (Oslo, 1994), p. 47.
2. W. P. Abbett and S. L. Hawley, *Astrophys. J.* **521**, 906 (1999).
<https://doi.org/10.1086/307576>
3. J. C. Allred, S. L. Hawley, W. P. Abbett, and M. Carlsson, *Astrophys. J.* **630**, 573 (2005).
<https://doi.org/10.1086/431751>

4. M. Carlsson, L. Fletcher, J. Allred, P. Heinzl, J. Kašparová, A. Kowalski, M. Mathioudakis, A. Reid, and P. J. A. Simões, *Astron. Astrophys.* **673**, A150 (2023).
<https://doi.org/10.1051/0004-6361/202346087>
5. D.-C. Song, J. Tian, Y. Li, M. D. Ding, Ya. Su, S. Yu, J. Hong, Ye. Qiu, Sh. Rao, X. Liu, Q. Li, X. Chen, Ch. Li, and Ch. Fang, *Astrophys. J. Lett.* **952**, L6 (2023).
<https://doi.org/10.3847/2041-8213/ace18c>
6. F. R. da Costa, *Proc. Int. Astron. Union* **12**, 94 (2016).
<https://doi.org/10.1017/S1743921317004021>
7. Ch. M. J. Osborne and L. Fletcher, *Mon. Not. R. Astron. Soc.* **516**, 6066 (2022).
<https://doi.org/10.1093/mnras/stac2570>
8. C. M. J. Osborne, P. Heinzl, J. Kašparová, and L. Fletcher, *Mon. Not. R. Astron. Soc.* **507**, 1972 (2021).
<https://doi.org/10.1093/mnras/stab2156>
9. Yu. A. Kupryakov, K. V. Bychkov, and O. M. Belova, *Izv. Krym. Astrofiz. Obs.* **119** (1), 19 (2023).
<https://doi.org/10.34898/izcrao-vol119-iss1-pp19-26>
10. L. M. Biberman, *Zh. Eksp. Teor. Fiz.* **17**, 416 (1947).
11. T. Holstein, *Phys. Rev.* **72**, 1212 (1947).
<https://doi.org/10.1103/physrev.72.1212>
12. T. Holstein, *Phys. Rev.* **83**, 1159 (1951).
<https://doi.org/10.1103/physrev.83.1159>
13. O. M. Belova and K. V. Bychkov, *Astrophysics* **61**, 224 (2018).
<https://doi.org/10.1007/s10511-018-9530-0>
14. Yu. A. Kupryakov, K. V. Bychkov, O. M. Belova, V. A. Maliutin, and A. B. Gorshkov, *Moscow Univ. Phys. Bull.* **79**, 275 (2024).
<https://doi.org/10.3103/s0027134924700334>

Publisher's Note. Allerton Press, Inc. remains neutral with regard to jurisdictional claims in published maps and institutional affiliations.

AI tools may have been used in the translation or editing of this article.